Dynamic Characteristics of Positive Pulsed Dielectric Barrier Discharge for Ozone Generation in Air*

WEI Linsheng (魏林生)[1,2], PENG Bangfa (彭邦发)[1], LI Ming (李鸣)[1], ZHANG Yafang (章亚芳)[1], HU Zhaoji (胡兆吉)[1]

[1]School of Resources, Environmental & Chemical Engineering, Nanchang University, Nanchang 330031, China
[2]Department of Mechanical and Aerospace Engineering, Florida Institute of Technology, FL 32901, USA

Abstract A comprehensive dynamic model consisting of 66 reactions and 24 species is developed to investigate the dynamic characteristics of ozone generation by positive pulsed dielectric barrier discharge (DBD) using parallel-plate reactor in air. The electron energy conservation equation is coupled to the electron continuity equation, the heavy species continuity equation, and Poisson's equation for a better description. The reliability of the model is experimentally confirmed. The model can be used to predict the temporal and spatial evolution of species, as well as streamer propagation. The simulation results show that electron density increases nearly exponentially in the direction to the anode at the electron avalanche. Streamer propagation velocity is about 5.26×10^4 m/s from anode to cathode in the simulated condition. The primary positive ion, negative ion, and excited species are O_2^+, O_3^- and $O_2(^1\Delta g)$ in pulsed DBD in air, respectively. N_2O has the largest density among nitrogen oxides. e and N_2^+ densities in the streamer head increase gradually to maximum values with the development of the streamer. Meanwhile, the O_2^+, O, O_3, $N_2(A^3\Sigma)$ and N_2O densities reach maximum values in the vicinity of the anode.

Keywords: dynamics, pulsed DBD, parallel-plate reactor, ozone, air

PACS: *52.80.−s, 52.30.−q, 52.65.−y*

DOI: 10.1088/1009-0630/18/2/09

(Some figures may appear in colour only in the online journal)

1 Introduction

As an environmentally friendly and powerful oxidant, ozone has been widely used in various applications, such as water treatment, air treatment, food storage, and chemical processing. However, high-energy consumption and low efficiency of ozone generation have become a serious problem that hinders the further development of ozone applications.

Some experimental investigations confirmed that pulsed dielectric barrier discharge (DBD) is a promising and highly efficient method of producing ozone. However, the dynamic characteristics of pulsed DBD remain unclear, which motivates the present research. Air and oxygen are two dominated gases for ozone production. The dynamic characteristics of the former are more complex than those of the latter. There are some investigations about discharge dynamics in air. For example, Fernadez-Rueda et al. [1] reported the radial distribution of species in a wire-cylinder reactor fed with air. They concluded that O_2^+ is the dominant positive ion inside the ionization region and O_3^- in the drift region. The ozone distributions in the vicinity of the wire in both wire-cylinder and wire-plate reactors were studied by Wang et al [2]. Chen et al. [3,4] investigated the ozone production in positive corona discharge and negative corona discharge using a wire-plate reactor. The result confirmed that the excited molecules of nitrogen and oxygen play an important role for ozone production. Meanwhile the ozone production rate in the negative corona is higher than that in the positive corona. To reveal the effect of water vapor on ozone generation, Ono [5] and Chen [6] added some reactions relating to water vapor into their models. They investigated ozone production dynamics using needle-plate and wire-plate configurations, respectively. Eliasson et al. [7] obtained the temporal evolution of species density in DBD with a parallel-plate reactor. Braun et al. [8] also tried to investigate dynamic characteristics, but only the temporal and spatial evolutions of electron and reduced electric field strength were shown. Most of the investigations about ozone generation dynamics focus on corona discharge with needle-plate, wire-plate, or wire-cylinder configurations. The dynamic characteristics of ozone generation in a parallel-plate chamber are also not well documented.

*supported by National Natural Science Foundation of China (Nos. 51366012 and 11105067), Jiangxi Province Young Scientists (Jinggang Star) Cultivation Plan of China (No. 20133BCB23008), Natural Science Foundation of Jiangxi, China (No. 20151BAB206047) and Jiangxi Province Higher School Science and Technology Landing Plan of China (No. KJLD-14015)

In this paper, a quasi-two-dimensional model of parallel-plate positive pulsed DBD in air is developed to investigate the dynamic characteristics of ozone generation. The validity of the model is confirmed by comparing with experimental data. And the temporal and spatial evolutions of important species are obtained. In addition, the characteristics of streamer propagation is analyzed.

2 Dynamic model

2.1 Computational domain and chemistry

The computational domain of this model is shown in Fig. 1. This model consists of four domains. They are a nickel-platinum high-voltage electrode of 0.4 mm in thickness, a ceramic plate with a thickness of 1 mm and a relative permittivity of 9 serving as the dielectric, an air gap of 1 mm and a stainless steel grounding electrode of 1 mm in thickness from top to bottom, respectively. The air in the gap is assumed to be composed of 21% oxygen and 79% nitrogen by volume. Triangulation is used as the mesh underlying the computational domains. Taking account of the quality of grid and computer power, we chose a finer grid for the gas gap domain and a coarse grid for the others.

Air discharge involves very complex physical and chemical phenomena. There are about 450 reactions among electrons, neutrals and ions in air discharge according to incomplete statistics. Different sets of reactions have been adopted in different models. For instance, Kossyi et al. [9] considered 266 reactions in their model and displayed the temporal variation of species density. The result showed that electronically excited nitrogen molecules and atoms play a significant role in nitrogen-oxygen plasmas. The model has a rather high demand for computation resources owing to the large number of reactions considered. To simplify, a model including 12 species and 24 reactions without charged species was built to analyze the process of ozone generation by positive corona discharge in air [3]. Ionikh [10] took 30 reactions and 14 species into account in his model, but no ions were included. As we know, charged species and ions are critical for ozone generation. To make the calculation more tractable, Hadji et al. [11] considered only five species and five reactions in their model to discuss the effect of N_2 concentration on ozone generation. This is to sacrifice the model fidelity to obtain a solution within computation resources.

In this paper, a reaction model consisting of 66 reactions and 24 species is developed to explore the distributions of electric field and species based on these previous researches [9,12−17]. The detailed reactions are presented in Table 1.

Reaction rate constants are expressed in s^{-1} for one-body reactions, in cm^3/s for two-body reactions and in cm^6/s for three-body reactions. T_e is electron temperature in eV. T_g is the gas temperature in K.

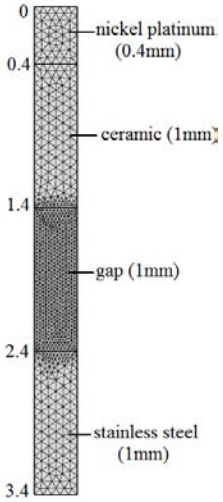

Fig.1 Computational domain

2.2 Governing equations

The essence of gas discharge is a series of reactions and motion of species. Usually, the continuity equation of species and Poisson's equation are adopted to describe the discharge process as reported by Soria [18], Yanallah [19,20], Loiseau [14], Komuro [21], and Eichwald [22]. However, the electron energy conservation equation is not included in their governing equations. As a matter of fact, electron energy is vital to revealing the mechanism of low-temperature, non-equilibrium plasma discharge [23]. It is because electron energy has a significant effect on the rate coefficient for electron impact ionization and excitation reactions and plays a pivotal role in electron mobility, diffusion coefficient, and thermal conductivity. To improve model description, the electron energy conservation equation is coupled to the electron continuity equation, the heavy species continuity equation and Poisson's equation as follows.

$$\frac{\partial n_e}{\partial t} + \nabla \cdot [-n_e(\mu_e \cdot \mathbf{E}) - D_e \cdot \nabla n_e] = R_e, \quad (1)$$

$$\frac{\partial n_\varepsilon}{\partial t} + \nabla \cdot [-n_\varepsilon(\mu_\varepsilon \cdot \mathbf{E}) - D_\varepsilon \cdot \nabla n_\varepsilon] = R_\varepsilon, \quad (2)$$

$$\rho \frac{\partial \omega_k}{\partial t} + \rho(\mathbf{u} \cdot \nabla)\omega_k = \nabla \cdot j_k + R_k, \quad (3)$$

$$-\nabla \cdot \varepsilon_0 \varepsilon_r \nabla V = \rho_q, \quad (4)$$

$$\rho_q = q(\sum_{k=1}^{N} Z_k n_k - n_e). \quad (5)$$

Here t is the time. n_e, n_ε and n_k are the densities of electron, electron energy, and heavy species, respectively. μ_e, μ_ε, D_e and D_ε represent the electron mobility, electron energy mobility, electron diffusivity, and electron energy diffusivity, respectively. R_e and R_ε are the electron chemical source term and electron energy source term, respectively. ρ is the density of the mixture. ρ_q is the space charge density. ω_k is the mass fraction of heavy particle. $\mathbf{u}$ is the mass average fluid velocity vector. j_k is the diffusive flux vector. R_k is the

Table 1. Reactions adopted in this model

No.	Reaction	Reaction rate constants (s^{-1}, cm^3/s or cm^6/s)	Reference
R1	$e+O_2 \Rightarrow O+O+e$	$f(E/N)$	[12]
R2	$e+O_2 \Rightarrow 2e+O_2^+$	$f(E/N)$	[12]
R3	$e+O_2 \Rightarrow O+O^-$	$f(E/N)$	[12]
R4	$e+O_2 \Rightarrow 2e+O+O^+$	$f(E/N)$	[12]
R5	$e+O_2 \Rightarrow O+e+O(^1D)$	$f(E/N)$	[12]
R6	$e+O_3 \Rightarrow O+O_2^-$	$f(E/N)$	[12]
R7	$e+O_2 \Rightarrow O_2(^1\Delta g)+e$	$f(E/N)$	[12]
R8	$e+O_2(^1\Delta g) \Rightarrow O+O+e$	$f(E/N)$	[12]
R9	$e+O_2 \Rightarrow O_2(^1\Sigma_g^+)+e$	$f(E/N)$	[12]
R10	$e+O_2(^1\Sigma_g^+) \Rightarrow e+O+O$	$f(E/N)$	[12]
R11	$e+N_2 \Rightarrow e+e+N_2^+$	$f(E/N)$	[13]
R12	$e+N_2 \Rightarrow e+N+N$	$f(E/N)$	[13]
R13	$e+N_2 \Rightarrow e+N_2(A^3\Sigma)$	$f(E/N)$	[13]
R14	$e+N_2 \Rightarrow e+N_2(B^3\Pi)$	$f(E/N)$	[13]
R15	$e+N_2 \Rightarrow e+N_2(C^3\Pi)$	$f(E/N)$	[13]
R16	$e+N_2 \Rightarrow e+N_2(a'^1\Sigma)$	$f(E/N)$	[13]
R17	$e+O_3 \Rightarrow O+O_2+e$	5.0×10^{-9}	[14]
R18	$e+O_2^+ \Rightarrow O+O(^1D)$	$2.2\times10^{-8}(T_e)^{-0.5}$	[12]
R19	$e+N_2^+ \Rightarrow N+N$	$8.3\times10^{-6}(T_e)^{-0.5}$	[13]
R20	$O+O_2+O_2 \Rightarrow O_3+O_2$	$6.9\times10^{-34}(300/T_g)^{1.25}$	[14]
R21	$O+O_3 \Rightarrow O_2+O_2$	$1.8\times10^{-11}\exp(-2300/T_g)$	[12]
R22	$O_2+O_3 \Rightarrow O+O_2+O_2$	$7.26\times10^{-10}\exp(-11400/T_g)$	[12]
R23	$O^-+O_2^+ \Rightarrow O+O_2$	$2.6\times10^{-8}(T_g/300)^{-0.44}$	[12]
R24	$O_2+O^+ \Rightarrow O+O_2^+$	2.1×10^{-11}	[12]
R25	$O_2+O^- \Rightarrow O+O_2^-$	3.2×10^{-10}	[12]
R26	$O_2^-+O_2^+ \Rightarrow O_2+O_2$	$2.01\times10^{-7}(T_g/300)^{-0.5}$	[12]
R27	$O(^1D)+O_3 \Rightarrow O+O_3$	2.5×10^{-10}	[12]
R28	$O+O_2+O_3 \Rightarrow O_3+O_3$	$1.45\times10^{-34}\exp(-663/T_g)$	[12]
R29	$O_2^-+O_3 \Rightarrow O_2+O_3^-$	7.8×10^{-10}	[12]
R30	$O^-+O_3 \Rightarrow O_2+O_3^-$	5.3×10^{-10}	[12]
R31	$O(^1D)+O_2 \Rightarrow O+O_2(^1\Sigma_g^+)$	$2.56\times10^{-11}\exp(-67/T_g)$	[12]
R32	$O_2^-+O_2^+ \Rightarrow O+O+O_2$	$1.01\times10^{-7}(T_g/300)^{-0.5}$	[12]
R33	$O_2^++O_3^- \Rightarrow O_3+O_2$	$2.0\times10^{-7}(T_g/300)^{-0.5}$	[12]
R34	$O_2^++O_3^- \Rightarrow O_3+O+O$	$1.01\times10^{-7}(T_g/300)^{-0.5}$	[12]
R35	$O_2^++O^- \Rightarrow O+O+O$	$2.6\times10^{-8}(T_g/300)^{-0.44}$	[12]
R36	$O(^1D)+O_2 \Rightarrow O+O_2$	$7.0\times10^{-12}\exp(67/T_g)$	[12]
R37	$O+O_2+N_2 \Rightarrow O_3+N_2$	$5.6\times10^{-29}(T_g)^{-2.0}$	[13]
R38	$N+O_2 \Rightarrow NO+O$	$1.1\times10^{-14}\times T_g\times\exp(-3150/T_g)$	[15]
R39	$N+NO \Rightarrow N_2+O$	$1.1\times10^{-12}(T_g)^{0.5}$	[13]
R40	$O_3+NO \Rightarrow NO_2+O_2$	$1.5\times10^{-12}\exp(-1300/T_g)$	[15]
R41	$O+NO_2 \Rightarrow NO+O_2$	$1.7\times10^{-11}\exp(-300/T_g)$	[15]
R42	$O_3+NO_2 \Rightarrow NO_3+O_2$	$1.2\times10^{-13}\exp(-2450/T_g)$	[15]
R43	$NO_3+NO_2 \Rightarrow N_2O_5$	3.8×10^{-12}	[15]
R44	$N_2O_5 \Rightarrow NO_3+NO_2$	$5.7\times10^{14}\exp(-10600/T_g)$	[15]
R45	$N+O_3 \Rightarrow NO+O_2$	5.7×10^{-13}	[15]
R46	$NO+NO_3 \Rightarrow NO_2+NO_2$	8.7×10^{-12}	[15]
R47	$N_2(A^3\Sigma)+O_2 \Rightarrow N_2+O+O$	1.7×10^{-12}	[13]
R48	$N_2(A^3\Sigma)+N_2(A^3\Sigma) \Rightarrow N_2+N_2(C^3\Pi)$	1.6×10^{-10}	[13]
R49	$N_2(B^3\Pi)+O_2 \Rightarrow N_2+O+O$	3.0×10^{-10}	[13]
R50	$N_2(B^3\Pi)+N_2 \Rightarrow N_2+ N_2(A^3\Sigma)$	3.0×10^{-11}	[13]
R51	$N_2(a'^1\Sigma)+N_2 \Rightarrow N_2+N_2$	2.0×10^{-13}	[13]
R52	$N_2(a'^1\Sigma)+O_2 \Rightarrow N_2+O+O(^1D)$	2.8×10^{-11}	[13]
R53	$N_2(C^3\Pi)+N_2 \Rightarrow N_2(B^3\Pi)+N_2$	1.0×10^{-11}	[13]
R54	$N_2(C^3\Pi)+O_2 \Rightarrow N_2(A^3\Sigma)+O+O$	3.0×10^{-10}	[13]
R55	$O_2+N_2^+ \Rightarrow N_2+O_2^+$	6.0×10^{-11}	[13]
R56	$N_2(A^3\Sigma)+O \Rightarrow NO+N^*(^2D)$	7.0×10^{-12}	[9]
R57	$N^*(^2D)+O_2 \Rightarrow NO+O$	$1.5\times10^{-12}(T_g/300)^{0.5}$	[9]
R58	$N_2(A^3\Sigma)+O_2 \Rightarrow N_2O+O$	7.8×10^{-14}	[9]
R59	$O+NO+N_2 \Rightarrow NO_2+N_2$	3.7×10^{-32}	[16]
R60	$O+NO+O_2 \Rightarrow NO_2+O_2$	3.7×10^{-32}	[16]
R61	$O+N+N_2 \Rightarrow NO+N_2$	$(1/35)\times5.03\times10^{-33}(T_g)^{-0.5}$	[16]
R62	$O+N+O_2 \Rightarrow NO+O_2$	$(1/35)\times5.03\times10^{-33}(T_g)^{-0.5}$	[16]
R63	$N_2O+ O(^1D) \Rightarrow 2NO$	7.2×10^{-11}	[9]
R64	$O+NO_2+N_2 \Rightarrow NO_3+N_2$	$9.0\times10^{-32}(T_g/300)^{-2}$	[17]
R65	$O+NO_2+O_2 \Rightarrow NO_3+O_2$	$9.0\times10^{-32}(T_g/300)^{-2}$	[17]
R66	$NO+NO+O_2 \Rightarrow NO_2+NO_2$	$3.3\times10^{-39}\exp(530/T_g)$	[17]

rate expression for heavy species k. ε_0 and ε_r are the vacuum permittivity and relative permittivity, respectively. q is the absolute value of electronic charge. Z_k is the electric charge. $\mathbf{E}$ is the electric field vector, V is the electric potential.

There are three mathematical methods to describe the physical phenomenon, namely the Partial Differential Equation, the Minimum Energy Problem, and the Weak Form. Among these methods, the Weak Form is considered to be the most suitable for solving nonlinear multi-physics problems since it has a minimum requirement on the continuity of integration variables. In the paper, Eqs. (1)-(5) are firstly transformed into a weak form, and then the Finite Element Method is used to obtain the numerical solution of each variable using the COMSOL Multiphysics package. Because of the high nonlinearity inherent in the drift diffusion equation, the electron number density can span 10 orders of magnitude over a very small distance. A better way of handling this equation, from a numerical point of view, is to solve for the log of the electron number and energy density, which facilitates the convergence of calculation. The calculation is implemented using a computer with a 3.40 GHz Intel(R) Core(TM) i7-4770 processor in 64-bit mode running in 16 GB memory, and requires about 2617 s for the code to be steady.

2.3 Boundary conditions

The boundary conditions are crucial for the computing process in this model. The boundary conditions for the equations are as follows:

a. The electron flux describing the scattering and absorption process of electrons at electrodes is [24]

$$\Gamma_e \cdot \mathbf{n} = \frac{1-\gamma_e}{1+\gamma_e}[-(2a_e-1)n_e\mu_e E\cdot n + \frac{1}{2}\nu_{e,th}n_e], \quad (6)$$

where Γ_e is the electron flux vector, $\mathbf{n}$ is the boundary normal vector and γ_e is the fraction of electrons reflected by the electrode. When the electron flux is directed toward the electrode, then a_e=1. Otherwise, it is equal to zero. $\nu_{e,th}$ is the electron thermal velocity.

b. The electron energy boundary condition at electrodes surface is expressed as [25]

$$\Gamma_\varepsilon \cdot \mathbf{n} = \frac{1}{3}\nu_{e,th}\bar{\varepsilon}n_e. \quad (7)$$

where Γ_ε is the electron energy flux vector, $\bar{\varepsilon}$ is the mean electron energy.

c. The boundary conditions for electron, electron energy, and heavy species at gap boundaries, namely the left and right sides of the gas gap, are given by

$$\begin{aligned} -\mathbf{n}\cdot\Gamma_e &= 0 \\ -\mathbf{n}\cdot\Gamma_\varepsilon &= 0, \\ -\mathbf{n}\cdot\Gamma_k &= 0 \end{aligned} \quad (8)$$

where Γ_k is the heavy species flux vector.

d. For the boundary conditions of neutral species, positive and negative ions, these heavy species decay into steady neutral species at the electrode surface and return into the discharge region [26], which is

$$\Gamma_k \cdot \mathbf{n} = \frac{\gamma_k}{4}\sqrt{\frac{8k_B T_k}{\pi m_k}}n_k. \quad (9)$$

where γ_k is the surface interaction coefficient, k_B is the Boltzmann's constant, T_k is the temperature for heavy species k, m_k is the mass for heavy species k.

e. A single pulsed voltage is applied on the top of the model, and the bottom of the model is grounded. The waveform of the pulsed voltage is presented in Fig. 2. The voltage begins at 1×10^{-7} s, then vanishes at 8.6×10^{-7} s.

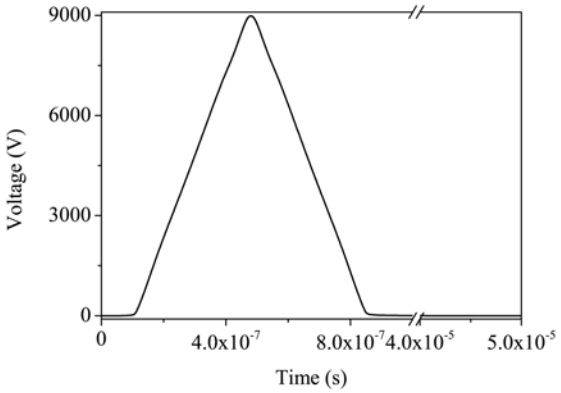

Fig.2 Waveform of the pulsed voltage

3 Results and discussion

3.1 Comparison between numerical and experimental results

Fig. 3 compares the numerical and experimental ozone concentrations for single positive pulsed DBD in air under atmospheric pressure. The detailed experiment is presented in a previous paper [27]. The experimental ozone concentration for single pulsed air discharge is obtained through dividing the total ozone concentration by the pulse numbers within the air residence time in the reactor. It can be seen from the figure that there is no big difference between simulation and experimental data, which confirms the validity of the model. It is noted that the simulation results are slightly higher than the experimental data. The reason is probably mainly that gas temperature will increase after applying continuous pulse power in the experiment, which is not favorable for ozone generation. On the contrary, a constant gas temperature of 293.15 K is assumed in the simulation. In addition, both the simulated and the experimental ozone concentrations increase with increasing peak voltage. More high-energy electrons will be produced to synthesize ozone because more electrical energy is injected into the reactor at a higher peak voltage with a constant pulse width.

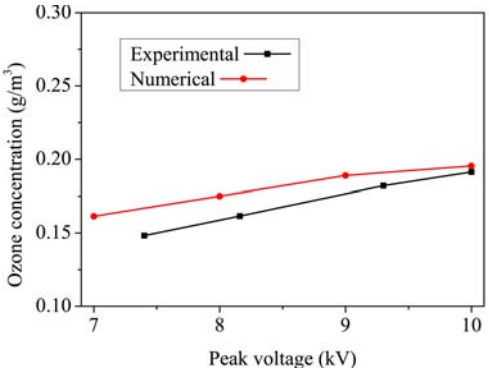

Fig.3 Numerical and experimental ozone concentration as a function of peak voltage

3.2 Temporal evolution of species concentrations

The temporal evolution of species concentrations is solved by the following equation:

$$\frac{\mathrm{d}[N]}{\mathrm{d}t} = \sum_i K_i c_i - \sum_j K_j c_j, \tag{10}$$

where $[N]$ is the concentration of any species; K is the reaction rate; c is the multiplication in concentration of reactive species for each reaction containing the species under the study, $c = \Pi_m[N_m], m = 1, 2, 3\ldots$; while i and j denote the reactions leading to the creation and the disappearance of the targeted species, respectively.

Fig. 4 presents the temporal evolution of charged species density at a peak voltage of 9 kV. The electron density reaches a peak of 3.58×10^{18} m^{-3} when ionization is maximal and then decreases dramatically as a result of recombination and attachment processes. The major positive ion is O_2^+ in the discharge, and its density is higher than N_2^+ density because the ionization of oxygen molecule is less than that of nitrogen molecule as reported by Benyamina et al [28]. O_2^+ density reaches a peak of 2.46×10^{18} m^{-3} at 4.5×10^{-7} s, and then reduces to one third because of the recombination and attachment processes as well as charge transfer reactions such as R24 and R55. O_3^- is the primary negative ion most of the time, but O_2^- density reaches the peak among all negative ions. The same conclusion was drawn for pure oxygen by Mennad [29]. O_3^- ions are formed via electron transfer reactions R29 and R30. Thus, it remains a high density after maximal ionization. The decreasing rate of O_2^- is much slower than that of O^-, O^+ and N_2^+, and O_2^- density is larger all the time. For O^-, O^+ and N_2^+, they reach sharp peaks and then decrease steeply owing to the charge transfer and recombination processes.

Fig. 5 illustrates the temporal evolution of neutral species density at a peak voltage of 9 kV. It shows that the O density reaches a maximum value of 2.28×10^{21} m^{-3} owing to the electron impact dissociation and then decreases as a result of the three-body collision reactions R20, R28, and R37 for ozone generation. Ozone density increases quickly at first and then becomes gradually stable. The stable ozone density is about 2.38×10^{21} m^{-3}. The process for stability needs about 10 μs which is longer than 3 μs in pure oxygen reported by Eliasson [30]. The difference lies in the presence of N_2 in our model because there are more complex reactions before achieving balance in air than in pure oxygen. N density reaches the peak and then follows a slight decrease due to the reaction with O_3. N_2O formed via R58 has the largest density among nitrogen oxides. Eliasson et al. [7] drew the same conclusion, but a different N_2O density was obtained owing to the different discharge parameters. NO density has a slight increase, and is less by about an order of magnitude than N_2O density. Additionally, other nitrogen oxides namely, NO_2, NO_3 and N_2O_5 are negligible.

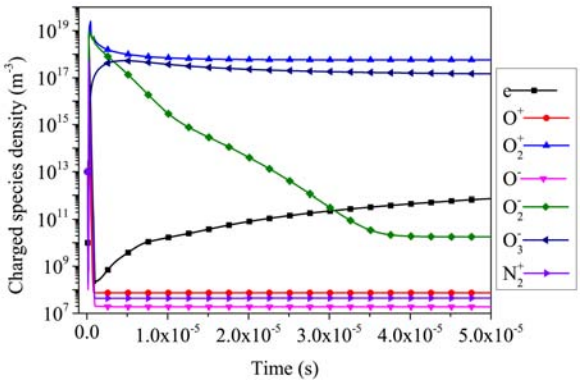

Fig.4 Temporal evolution of charged species density

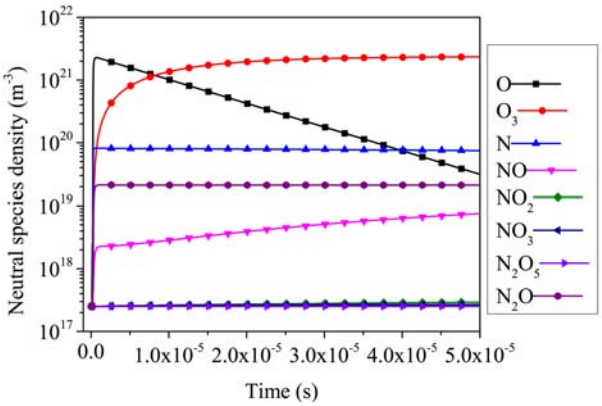

Fig.5 Temporal evolution of neutral species density

Fig. 6 shows the temporal evolution of excited species density. It is apparent from the figure that the primary excited species are $O_2(^1\Delta g)$ and $O_2(^1\Sigma_g^+)$ generated by electron impact excitation, and their maximal densities are 2.99×10^{20} m^{-3} and 1.18×10^{20} m^{-3}, respectively. All other excited species fall dramatically after maximal ionization. For example, $O(^1D)$ density goes up steeply via electron impact dissociation (reaction R5), and then drops sharply, resulting from reactions R31 and R36. Comparing Fig. 5 and Fig. 6, it can be seen that the rate of decrease of $O(^1D)$ is much faster than that of O because of significant differences between the reaction rates for the consumption reactions of O(1D) and O. Meanwhile, some heavy particles-related reactions may still produce O although high-energy electrons decrease. Excited nitrogen molecules

present the same behavior. $N_2(A^3\Sigma)$ achieves the highest density of 1.8×10^{20} m^{-3} among all excited nitrogen molecules. The sharp decline of $N_2(A^3\Sigma)$ results from reactions R47, R48, R56, and R58. Reaction R57 leads to the dramatic decrease of $N^*(^2D)$ produced by excitation reaction R56. Peyrous [17] observed the same tendencies about some species such as O_3, O, NO and N_2O in corona discharge.

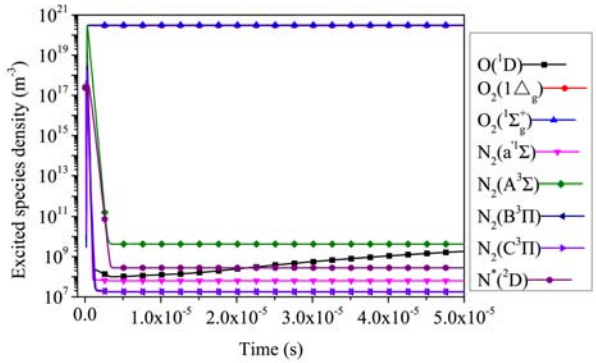

Fig.6 Temporal evolution of neutral species density

3.3 Spatial distribution of electron and charged species density at electron avalanche

The distribution of electrons at 2.35×10^{-7} s is presented in Fig. 7. Electrons are accelerated toward the anode and ionize neutral species under the effect of the electric field. Due to the electron avalanche, the electron density increases nearly exponentially in the direction to the anode (see the fitting curve in Fig. 7). Fig. 8 shows the electron density distribution along the y-axis in the vicinity of the anode from this study and Yanallah et al [31]. A similar behavior was observed by Yanallah et al. for an anode of 0.04 mm, here the electron density difference results from the difference in electric field strength. The principal source of electrons is the direct ionization of oxygen and nitrogen molecules, namely reactions R2, R4 and R11.

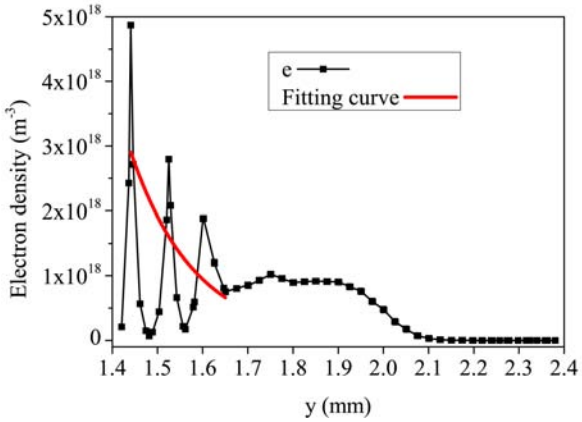

Fig.7 Electron density distribution along the y-axis

The ionization reactions are drastic because electrons gain most of energy in the anode region, and the electron density reaches a maximum value in the vicinity of the anode. It is interesting to note that the electron density fluctuates in the anode region. The reason is that electrons need relaxation time to obtain enough energy again because of the increasing rates of electrons collision with heavy species when the number and energy of electrons increase. Moreover, electron attachment reactions are more likely to occur when a part of the electron energy has been transferred into heavy species.

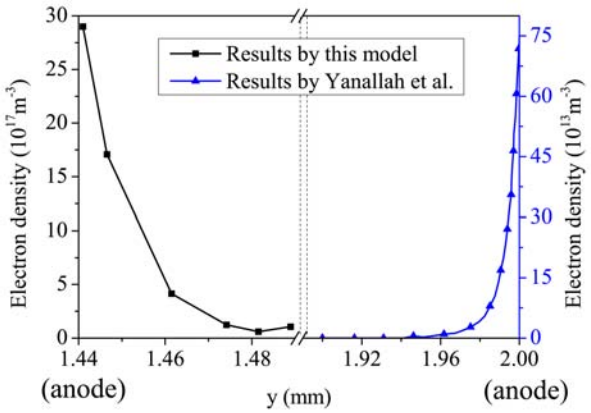

Fig.8 Electron density distribution along the y-axis in the vicinity of the anode from this study and Yanallah et al. [31]

Most of the negative ions are produced by electrons attachment to neutral molecules. Thus, the distributions of negative ions are extremely similar to that of electron as shown in Fig. 9(a). The principal reactions contributing to the formation of O_2^- and O^- are reactions R3, R6 and R25. The ozone concentration is low at the time of electron avalanche. Therefore, it is limited to generate O_2^- by means of R6. The majority of the O_2^- ions have been formed by reaction R25. O_3^- ions come from O_2^- and O^- via electron transfer reactions R29 and R30. Its density is also insignificant because there is not enough O_3 for reactions R29 and R30. The peaks of O_3^- density correspond to the troughs of O_2^- and O^- densities owing to the fact that some O_2^- and O^- ions have been transformed into O_3^-. Furthermore, O_2^- and O^- ions may react and transform into other species such as O and O_2.

Positive ions generated near the anode are formed by ionization reactions R2, R4 and R11. As a result, the distributions of positive ions are similar to that of the electron as presented in Fig. 9(b). O_2^+ is the most principal positive ion at the electron avalanche, and it has a higher density than O^+ and N_2^+. There are two reasons: 1) Reaction R2 has a lower threshold energy than reactions R5 and R11; and 2) O^+ and N_2^+ ions are efficiently converted into O_2^+ because of the presence of fast charge transfer reactions R24 and R55. With the development of electron avalanche, these existing positive and negative ions will disappear via recombination reactions R19, R23, R26, and R32-R35.

3.4 Streamer propagation

Fig. 10 shows the 2D spatial distribution of the electric field during streamer propagation. As can be seen from Fig. 10(a) and (b), a weak streamer in the gas gap

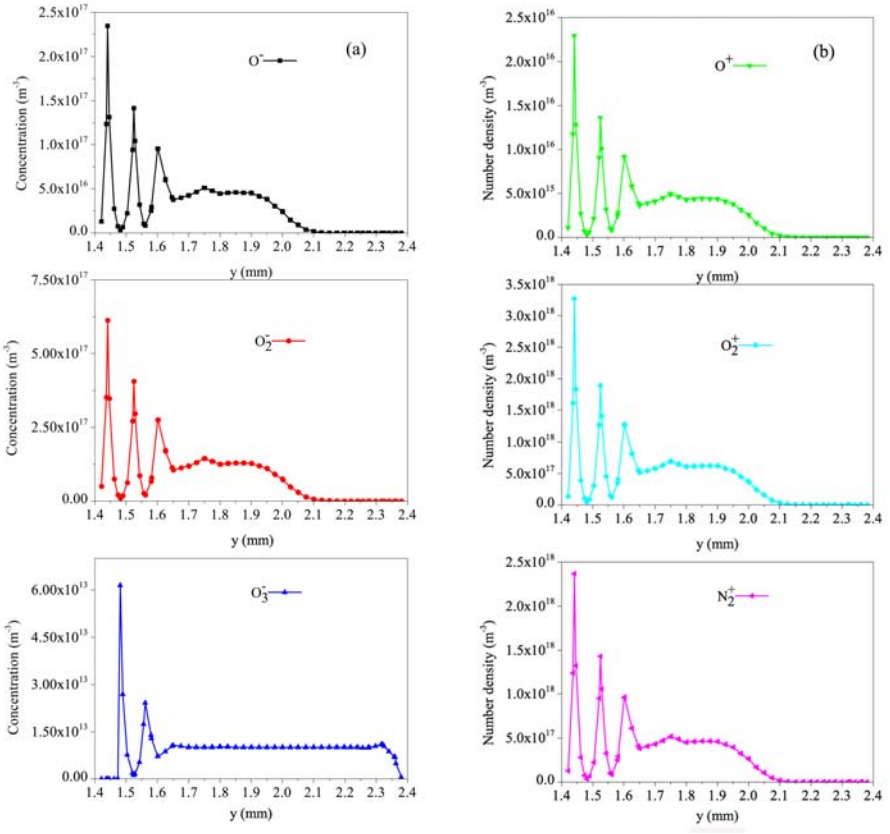

Fig.9 Charged ions distribution of (a) negative ions and (b) positive ions along the y-axis

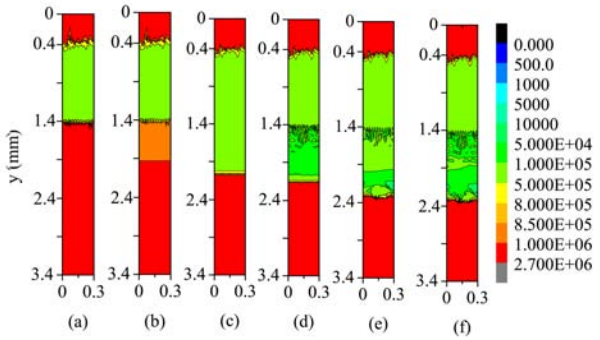

Fig.10 2D spatial distribution of electric field at 9 kV and different times of (a) 2.35×10^{-7} s, (b) 2.36×10^{-7} s, (c) 2.42×10^{-7} s, (d) 2.48×10^{-7} s, (e) 2.55×10^{-7} s and (f) 2.56×10^{-7} s

begins to appear at 2.36×10^{-7} s, and there is no obvious streamer until 2.36×10^{-7} s because the electron avalanche has not sufficiently developed to convert into a streamer. The streamer initiates from the anode and moves towards the cathode. The electron field of the streamer head is gradually strengthened by accelerated electron-impact reactions during streamer propagation as shown in Fig. 10(c) and (d). Comparing Fig. 10(e) and (f), it is clear that the streamer head does not move any more at 2.55×10^{-7} s. Therefore, the streamer bridges the whole gas gap in 19 ns, and its average velocity is approximate 5.26×10^{4} m/s. There are oscillations in Fig. 10 which may be caused by grids and different materials. Wan et al. [32] investigated the process of streamer propagation in a coaxial cylindrical reactor in air under atmospheric pressure. They found that the streamer propagation velocity is 8×10^{5} m/s for a peak voltage of 43 kV, and is about one order of magnitude larger than our result. It seems a reasonable explanation that a higher peak voltage leads to a higher streamer propagation velocity because streamer propagation velocity increases with increasing peak voltage. Moreover, the streamer propagation velocity may differ by up to an order of magnitude under similar conditions [33].

3.5 Distribution of e, O_2^+ and N_2^+

Electrons are the energy carrier in streamer discharge because the nature of the discharge is a process of electron-impact reactions such as ionization and excitation. Therefore, investigation on electron profile is extremely important for comprehensive understanding of the chemical and physical mechanism in streamer discharge. Furthermore, electrons generation is closely related to O_2^+ and N_2^+.

The electron density distributions in pulsed DBD are depicted in Figs. 11(a) and 12(a), which show that there exist a peak value of electron density in the vicinity of the anode and streamer head. The electron density in the streamer head increases gradually to a maximum value with the development of the streamer because more collision ionization reactions occur between the molecules and electrons in the streamer head to produce more electrons. Meanwhile the electron density in the vicinity of the anode increases at first accompanying the electron avalanche and then weakens gradually. The electron density almost remains constant

at any given time in the streamer channel because the streamer channel can be regarded as the plasma channel after the steamer moves away. Then the change of the electron density with time in the streamer channel is the same as that in the vicinity of the anode. Electrons decrease quickly near two interfaces because electrons will be scattered and absorbed by electrodes. Because most electrons are formed by means of ionization reactions R2 and R11 while O_2^+ and N_2^+ are generated, the density distributions of O_2^+ and N_2^+ are similar to that of the electron as presented in Fig. 11(b), Fig. 11(c), Fig. 12(b), and Fig. 12(c), respectively. However, there is a slight discrepancy between O_2^+ and electron in that the O_2^+ density along the whole y-axis increases with the development of streamer and reaches the maximum value in the vicinity of the anode. This is because the production rate of O_2^+ is larger than its consumption rate and O_2^+ does not migrate timely to the cathode in the discharge space.

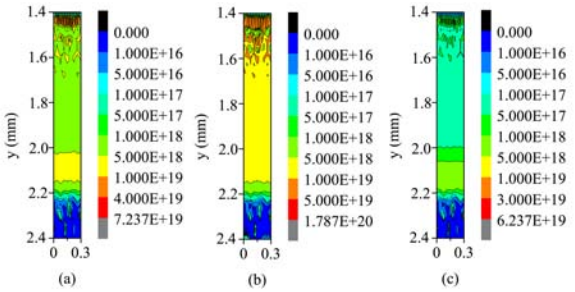

Fig.11 2D spatial distribution of (a) electron, (b) O_2^+, and (c) N_2^+ at 2.48×10^{-7} s

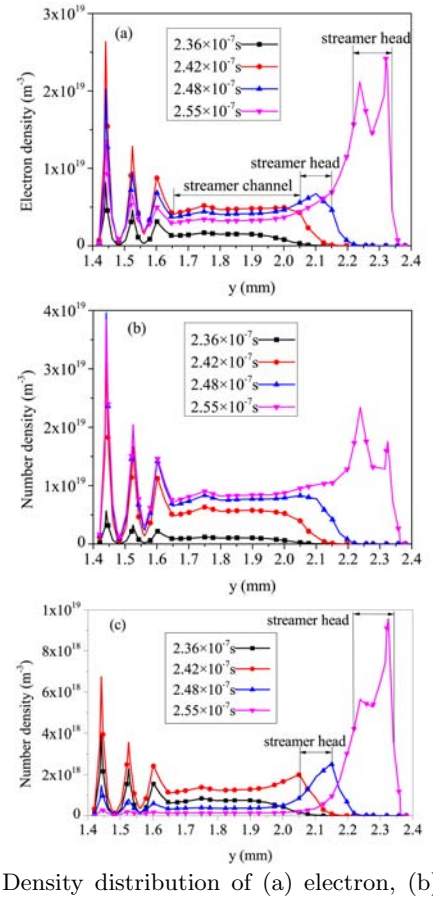

Fig.12 Density distribution of (a) electron, (b) O_2^+ and (c) N_2^+ along the y-axis

3.6 Distribution of O and O_3

The density distributions of O and O_3 in pulsed DBD are shown in Figs. 13 and 14. O and O_3 are mainly produced through the reactions below:

$$e + O_2 => O + O + e \quad (6.0\ eV) \quad (R1)$$

$$e + O_2 => e + O + O(^1D) \quad (8.4\ eV) \quad (R5)$$

$$O + O_2 + O_2 => O_2 + O_3 \quad (R20)$$

$$O + O_2 + N_2 => N_2 + O_3 \quad (R37)$$

These reactions strongly depend on the electron, so the density distributions of O and O_3 have a similar behavior to that of the electron. However, there are two differences between them. The first is that the densities of O and O_3 increase steadily in the discharge space. This is because the applied voltage is still rising in the applied pulsed voltage during streamer propagation. The energy input into the discharge process therefore increases and more high-energy electrons are produced which in turn produce more O and O_3. The second is that the maximum values of O and O_3 densities take place near the anode throughout streamer propagation because most high energy electrons exist in this area. It is also noted that O_3 grows slower than O in the direction of streamer propagation because O is the precursor of O_3 and needs time to transform into O_3. In addition, a relatively smaller peak density of O appears in the vicinity of the cathode at 2.55×10^{-7} s.

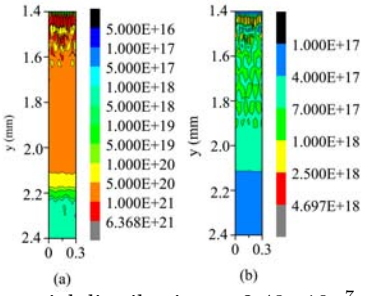

Fig.13 2D spatial distribution at 2.48×10^{-7} s: (a) O, and (b) O_3

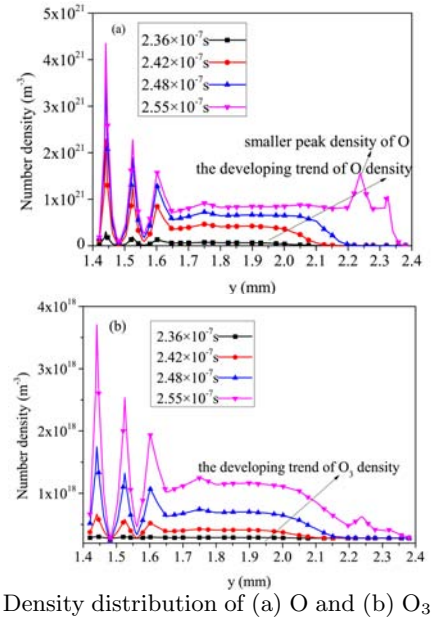

Fig.14 Density distribution of (a) O and (b) O_3 along the y-axis

3.7 Distribution of $N_2(A^3\Sigma)$ and N_2O

The density distributions of $N_2(A^3\Sigma)$ and N_2O in pulsed DBD are displayed in Figs. 15 and 16. $N_2(A^3\Sigma)$ and N_2O behave like O and O_3 because all of them strongly depend on the electron. The excited species $N_2(A^3\Sigma)$ is formed via the following reactions

$$e + N_2 => N_2(A^3\Sigma) + e \quad (R13)$$

$$N_2(B^3\Pi) + N_2 => N_2 + N_2(A^3\Sigma) \quad (R50)$$

$$N_2(B^3\Pi) + O_2 => O + O + N_2(A^3\Sigma) \quad (R54)$$

Additionally, $N_2(B^3\Pi)$ is also formed by the direct electron impact excitation reaction of nitrogen molecules. Thus the total concentration of $N_2(A^3\Sigma)$ increases with streamer propagation as a result of the rising electron density. For N_2O, the collision of $N_2(A^3\Sigma)$ with O_2 is a main source.

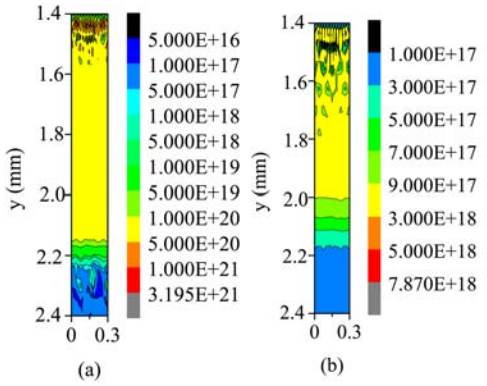

Fig.15 2D spatial distribution at t=2.48×10^{-7} s: (a) $N_2(A^3\Sigma)$, and (b) N_2O

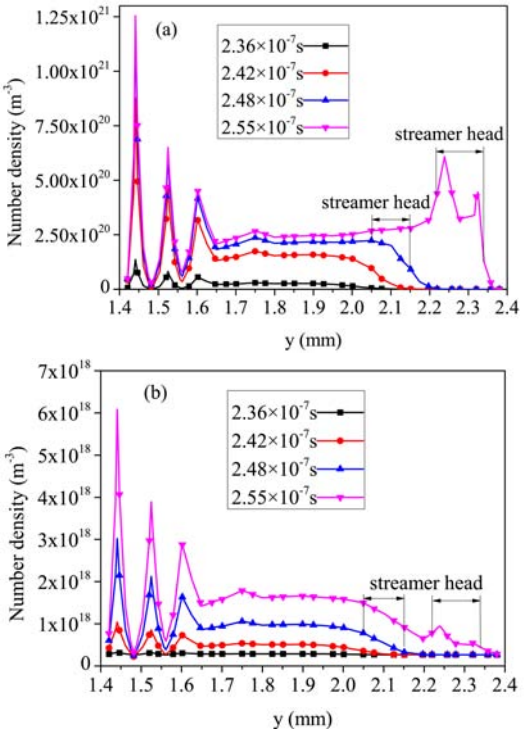

Fig.16 Density distribution of (a) $N_2(A^3\Sigma)$ and (b) N_2O along the y-axis

$$N_2(A^3\Sigma) + O_2 => O + N_2O \quad (R58)$$

That is why the density distribution of N_2O is similar to that of $N_2(A^3\Sigma)$. Like O and O_3, $N_2(A^3\Sigma)$ is the precursor of N_2O, so N_2O has a slower change than $N_2(A^3\Sigma)$.

4 Conclusion

A relatively comprehensive dynamic model consisting of 66 reactions and 24 species is developed to study positive pulsed DBD using a parallel-plate reactor in air under atmospheric pressure. For a better description, the electron energy conservation equation is coupled to the electron continuity equation, the heavy species continuity equation and Poisson's equation. The ozone concentrations predicted by the model are in good agreement with experimental results. Several conclusions can be made as follows:

a. According to the temporal evolution of species density, the primary positive ion, and negative ion, excited specie are O_2^+, O_3^- and $O_2(^1\Delta g)$ in pulsed DBD in air, respectively. Ozone reachs a peak of about 2.38×10^{21} m^{-3}. Additionally, N_2O has the largest density among nitrogen oxides. The change trends of some species are in agreement with those in published literature, with discrepancies arising from differences in the models.

b. It is apparent from the charged species distribution along the y-axis at electron avalanche that electron density increases nearly exponentially in the direction to the anode. With the development of the electron avalanche, a streamer emerges from the anode and reaches the cathode within 19 ns. The average velocity is about 5.26×10^4 m/s.

c. Density distributions of main species are obtained during streamer propagation. It is concluded that e and N_2^+ densities in the streamer head increase gradually to maximum values with the development of the streamer. Meanwhile, the O_2^+, O, O_3, $N_2(A^3\Sigma)$ and N_2O densities reach maximum values in the vicinity of the anode.

References

1 Fernandez-Rueda A, Pontiga F, Soria C, et al. 2005, Numerical simulation of wire-to-cylinder negative corona discharge in dry air. 2005 Annual Report Conference on Electrical Insulation and Dielectric Phenomena, Nashville, Tennessee, USA
2 Wang P, Chen J. 2009, J. Phys. D: Appl. Phys., 42: 035202
3 Chen J, Davidson J H. 2002, Plasma Chem. Plasma Process., 22: 495
4 Chen J, Davidson J H. 2003, Plasma Chem. Plasma Process., 23: 501
5 Ono R, Oda T. 2003, J. Appl. Phys., 93: 5876
6 Chen J, Wang P. 2005, IEEE Trans. Plasma Sci., 33: 808

7 Eliasson B, Kogelschatz U. 1991, IEEE Trans. Plasma Sci., 19: 309
8 Braun D, Pietsch G. 1991, J. Phys. D: Appl. Phys., 24: 564
9 Kossyi I, Kostinsky A Y, Matveyev A, et al. 1992, Plasma Sources Sci. Technol., 1: 207
10 Ionikh Y, Meshchanov A, Röpcke J, et al. 2006, Chem. Phys., 322: 411
11 Hadji K, Hadji A, Hadj-Ziane S, et al. 2008, Plasma Devices Oper., 16: 75
12 Eliasson B, Kogelschatz U. 1986, Basic data for modelling of electrical discharges in gases: oxygen. ABB Asea Brown Boveri, Baden, German
13 Poggie J, Adamovich I, Bisek N, et al. 2013, Plasma Sources Sci. Technol., 22: 015001
14 Loiseau J, Lacassie F, Monge C, et al. 1994, J. Phys. D: Appl. Phys., 27: 63
15 Yagi S, Tanaka M. 1979, J. Phys. D: Appl. Phys., 12: 1509
16 Pintassilgo C, Loureiro J, Guerra V. 2005, J. Phys. D: Appl. Phys., 38: 417
17 Peyrous R. 1990, Ozone-Sci. Eng., 12: 41
18 Soria C, Pontiga F, Castellanos A. 2004, Plasma Sources Sci. Technol., 13: 95
19 Yanallah K, Pontiga F, Castellanos A. 2011, J. Phys. D: Appl. Phys., 44: 055201
20 Yanallah K, Pontiga F, Fernandez-Rueda A, et al. 2009, J. Phys. D: Appl. Phys., 42: 065202
21 Komuro A, Ono R, Oda T. 2012, J. Phys. D: Appl. Phys., 45: 265201
22 Eichwald O, Ducasse O, Dubois D, et al. 2008, J. Phys. D: Appl. Phys., 41: 234002
23 Ebert U, Sentman D D. 2008, J. Phys. D: Appl. Phys., 41: 230301
24 Hagelaar G, De Hoog F, Kroesen G. 2000, Phys. Rev. E, 62: 1452
25 Boeuf J, Pitchford L. 1995, Phys. Rev. E, 51: 1376
26 Farouk T, Farouk B, Staack D, et al. 2006, Plasma Sources Sci. Technol., 15: 676
27 Wei L S, Yuan D K, Zhang Y F, et al. 2014, Vacuum, 104: 61
28 Benyamina M, Belasri A, Khodja K. 2014, Ozone-Sci. Eng., 36: 253
29 Mennad B, Harrache Z, Aid D A, et al. 2010, Curr. Appl. Phys., 10: 1391
30 Eliasson B, Hirth M, Kogelschatz U. 1987, J. Phys. D: Appl. Phys., 20: 1421
31 Yanallah K, Pontiga F, Chen J. 2013, J. Phys. D: Appl. Phys., 46: 345202
32 Wang D, Jikuya M, Yoshida S, et al. 2007, IEEE Trans. Plasma Sci., 35: 1098
33 Won J Y, Williams P. 2002, J. Phys. D: Appl. Phys., 35: 205

(Manuscript received 16 March 2015)
(Manuscript accepted 16 June 2015)
E-mail address of WEI Linsheng:
weilinsheng@ncu.edu.cn